mater.scichina.com link.springer.com

Published online 9 November 2023 | https://doi.org/10.1007/s40843-023-2627-0
Sci China Mater 2023, 66(12): 4669–4679

Rod-shaped aggregates of sulfur-doped carbon nitride nanosheets for enhanced photocatalytic hydrogen evolution

Siying Lin[1], Baogang Wu[1], Qi Li[2], Xudong Xiao[1], Mang Zheng[2], Jianan Liu[1], Ying Xie[1] and Baojiang Jiang[1*]

ABSTRACT **Synthesis of few-layer carbon nitride with wide absorption spectra is an interesting research area. Heteroatom doping, particularly sulfur (S) doping, can effectively prevent band gap widening triggered by the quantum confinement effect in nanoscale carbon nitride sheets. Herein, different from that in second calcination sulfuration, the presulfuration supramolecular precursors can *in situ* form the S-doped carbon nitride (SCN) nanosheet stacked microrods. This few-layer frame construction possesses a large specific surface area (139.06 $m^2 g^{-1}$), exposes more active sites, and facilitates the internal reflection of photons. Furthermore, the introduction of S distorts the conjugated structure of the original heptazine ring, narrowing the band gap of carbon nitride through the activation of the n→π* transition in valence band electrons. Consequently, the light absorption range is extended to 700 nm. Finally, the hydrogen evolution rate of $SCN_{0.8}$ (3925.8 μmol $g^{-1} h^{-1}$) is 8.1 times that of bulk carbon nitride (485.2 μmol $g^{-1} h^{-1}$) under simulated sunlight conditions (AM 1.5G). The stacking of sheets avoids the accumulation of nanosheets and enhances performance and structural stability. The proposed structure aims to maximize the utilization of synergistic effects of heteroatom doping and morphology regulation to improve photocatalytic hydrogen evolution. Furthermore, this work provides a new perspective for the multidimensional synchronous optimization of photocatalysts.**

Keywords: sulfur-doped carbon nitride, few-layer, supramolecular self-assembly, photocatalysis, hydrogen evolution

INTRODUCTION

As a polymer semiconductor, graphitic carbon nitride ($g-C_3N_4$) has immense potential in photocatalysis owing to its physicochemical robustness, environmental nontoxicity, uncomplicated synthesis, and appropriate energy band [1–3]. The efficiency of photocatalytic applications of bulk carbon nitride (BCN) is limited by several factors, including a deficiency in active sites, a high rate of charge recombination, a low carrier transfer efficiency, and a narrow absorption range [4–7]. In recent years, morphological regulation, element doping, and heterogeneous structure construction have been used to optimize the structure of $g-C_3N_4$ for different photocatalytic applications, such as photocatalytic hydrogen evolution [8–13]. Among them, the morphology regulation of $g-C_3N_4$ has been proven to be efficient for photocatalytic water splitting [14–17]. Specifically, the ultrathin $g-C_3N_4$ structure can fully expose active sites and facilitate charge and mass transfer, thereby enhancing the photocatalytic efficiency [18–21]. However, the ultrathin $g-C_3N_4$ generally has a wider band gap than BCN due to the quantum restriction effect [22]. Introducing heteroatoms into the $g-C_3N_4$ skeleton is a promising approach to narrow the band gap. Moreover, the heteroatom sites can act as charge-trapping sites and prevent their recombination [23–25]. Compared with metal doping, nonmetallic doping can avoid structural sharp damage of $g-C_3N_4$ caused by thermal changes in the chemical states of metal ions [26–30]. Therefore, doping of nonmetallic elements, such as sulfur (S) [31,32], phosphorus (P) [33,34], carbon (C) [35,36], oxygen (O) [37,38], and boron (B) [39,40], on $g-C_3N_4$ has recently emerged as a prominent research focus. Specifically, S-doped $g-C_3N_4$ has been proven to considerably enhance visible-light absorption and narrow the band gap [41,42].

Theoretically, the simultaneous modulation of morphology and S doping optimize the surface reaction and light absorption of carbon nitride [43–45]. However, a simple, balanced strategy is still lacking. Earlier studies have revealed that the hard/soft template method can be used to prepare $g-C_3N_4$ with hierarchical micro/nanostructures [46–48]. The aforementioned method involves a complex experimental procedure accompanied by high cost, which may potentially compromise the integrity of the ultrathin $g-C_3N_4$ framework during template removal. The supramolecular precursor strategy is a straightforward and template-free approach for synthesizing S-doped $g-C_3N_4$ with a uniformly distributed lamellar structure. Inspired by previous studies, we found that the products synthesized from different raw materials have different characteristics [49]. Particularly, because of the similar molecular structures of thiourea (TU) and urea, carbon nitride calcined with urea precursor exhibits a high specific surface area [50]. Moreover, TU is an effective precursor for synthesizing S-doped $g-C_3N_4$. This method permits band structure modulation without requiring the introduction of extra heteroatoms [51]. Moreover, ethanol exhibits high solubility for urea and TU. Under appropriate conditions, these raw materials can undergo self-assembly into regular, sulfurated, rod-shaped precursors.

Herein, we fabricated rod-shaped aggregates of S-doped carbon nitride (SCN) nanosheet using a supramolecular self-assembly method and achieved cooperative optimization of

[1] School of Chemistry and Materials Science, Heilongjiang University, Harbin 150080, China
[2] College of Materials Science and Chemical Engineering, Harbin Engineering University, Harbin 150001, China
* Corresponding author (email: jbj@hlju.edu.cn)

morphology regulation and light absorption. Urea, TU, and cyanuric acid were selected as the raw materials for the precursor synthesis. After calcination and polycondensation, S atoms are *in situ* doped into the framework of g-C_3N_4. Because of the new energy level produced by the S introduction, the band gap of SCN is considerably reduced to 2.51 eV, which perfectly compensates for the band gap widening caused by the quantum restriction effect. Therefore, adjusting the band structure of g-C_3N_4 is feasible by introducing nonmetallic atoms [52–56]. Moreover, the rod-shaped aggregate formed *via* stacking special sheets renders $SCN_{0.8}$ a large specific surface area (139.06 $m^2 g^{-1}$). The results demonstrate that under simulated illumination conditions (AM1.5), the photocatalytic hydrogen evolution efficiency of $SCN_{0.8}$ is 3925.8 μmol $g^{-1} h^{-1}$, which is 8.1 times that of BCN (485.2 μmol $g^{-1} h^{-1}$). The supramolecular self-assembly technology offers a viable and promising approach for fabricating g-C_3N_4 photocatalysts with element doping, multilayer morphology, and exceptional performance.

EXPERIMENTAL SECTION

Materials

Cyanuric acid ($C_3H_3N_3O_3$), urea (CH_4N_2O), TU (CH_4N_2S), ethanol (C_2H_5OH), and lactic acid ($C_3H_6O_3$) were obtained from Aladdin Chemical Reagent Co., Ltd. All chemicals used were of analytical grade and used as received without further purification.

Preparation of SCN samples

First, 0.67 g of urea (11 mmol) was dissolved in 50 mL of ethanol at 80°C. After rapidly stirring for 30 min, $x \times 11$ mmol (x = 0, 0.4, 0.8, or 1.6; x represents the molar ratios of TU and urea) of TU was added into the above solution. The reaction system was stirred for 30 min at 80°C. Subsequently, 0.5 g of cyanuric acid was added to the above solution at 80°C, and stirred for 60 min. Afterward, the suspension was poured into a 100-mL Teflon-lined autoclave and heated at 180°C for 12 h. The mixture was centrifuged, washed with ethanol, and placed in the vacuum drying equipment at 60°C for 12 h. Finally, the resultant solids were heated to 500°C for 2 h under nitrogen flow with a heating rate of 5°C min^{-1}. The resulting materials were referred to as SCN_0, $SCN_{0.4}$, $SCN_{0.8}$, and $SCN_{1.6}$.

Preparation of BCN

The melamine was calcined to 500°C with a heating rate of 5°C min^{-1} in a tube furnace under nitrogen flow and kept at 500°C for 2 h. After cooling, a comparative sample was obtained, which was named BCN.

RESULTS AND DISCUSSION

Scheme 1 illustrates the synthesis of SCN through the self-assembly of ternary precursor molecules. Initially, urea and TU with varying masses were dissolved in an ethanol solution, followed by the addition of cyanuric acid. The resulting mixed solution was then transferred to a Teflon-lined autoclave and reacted at 180°C for 12 h. Consequently, supramolecular aggregates were obtained *via* the self-assembly method using these three substances. Subsequently, these aggregates were heated at a rate of 5°C min^{-1} in a nitrogen atmosphere up to 500°C for 2 h. The materials obtained from this process were designated as SCN. The pyrolysis of these supramolecular precursors imparts SCN with a S-doped molecular structure and reduces its number of layers.

Scanning electron microscopy (SEM) images (Fig. 1a and Fig. S1) reveal that the precursor of $SCN_{0.8}$ has a rod-shaped morphology with a width of 2–8 μm and a length of >50 μm. After calcination, the obtained $SCN_{0.8}$ exhibits a lamellar morphology (Fig. 1b) due to the continuous gas release during pyrolysis. The edge distortion of sheets (Fig. 1c) reduces the surface energy. Notably, the morphology of $SCN_{0.8}$ with the open surface and abundant curled sheets facilitates the exposure of reaction sites, accelerates charge separation, and promotes interface mass transfer, thereby beneficial for enhancing photocatalytic performance. Furthermore, transmission electron microscopy (TEM) image reveals the twisted ultrathin nanosheet morphology of $SCN_{0.8}$ (Fig. 1d), which suppresses interlayer tight stacking. A thickness of 3.7 nm (Fig. 1e, f) of the nanosheets was randomly measured using atomic force microscopy (AFM). The distribution of C, N, O, and S on the $SCN_{0.8}$ surface was observed to be even, as shown in Fig. 1g and Fig. S2. Energy-dispersive X-ray spectroscopy (EDX) and the corresponding elemental mapping reveal that S atoms exhibit the same dispersibility as C, N and O. The SEM and TEM images of BCN and $SCN_{0.8}$ (Figs S3 and S4) reveal that $SCN_{0.8}$ exhibits a rod-shaped structure comprising nanosheets compared with BCN. This unique morphological feature favors photogenerated

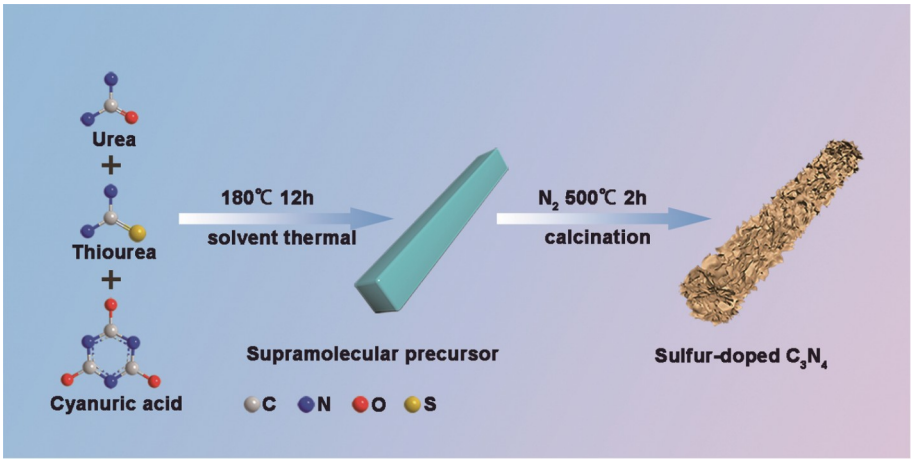

Scheme 1 Formation mechanism of SCN.

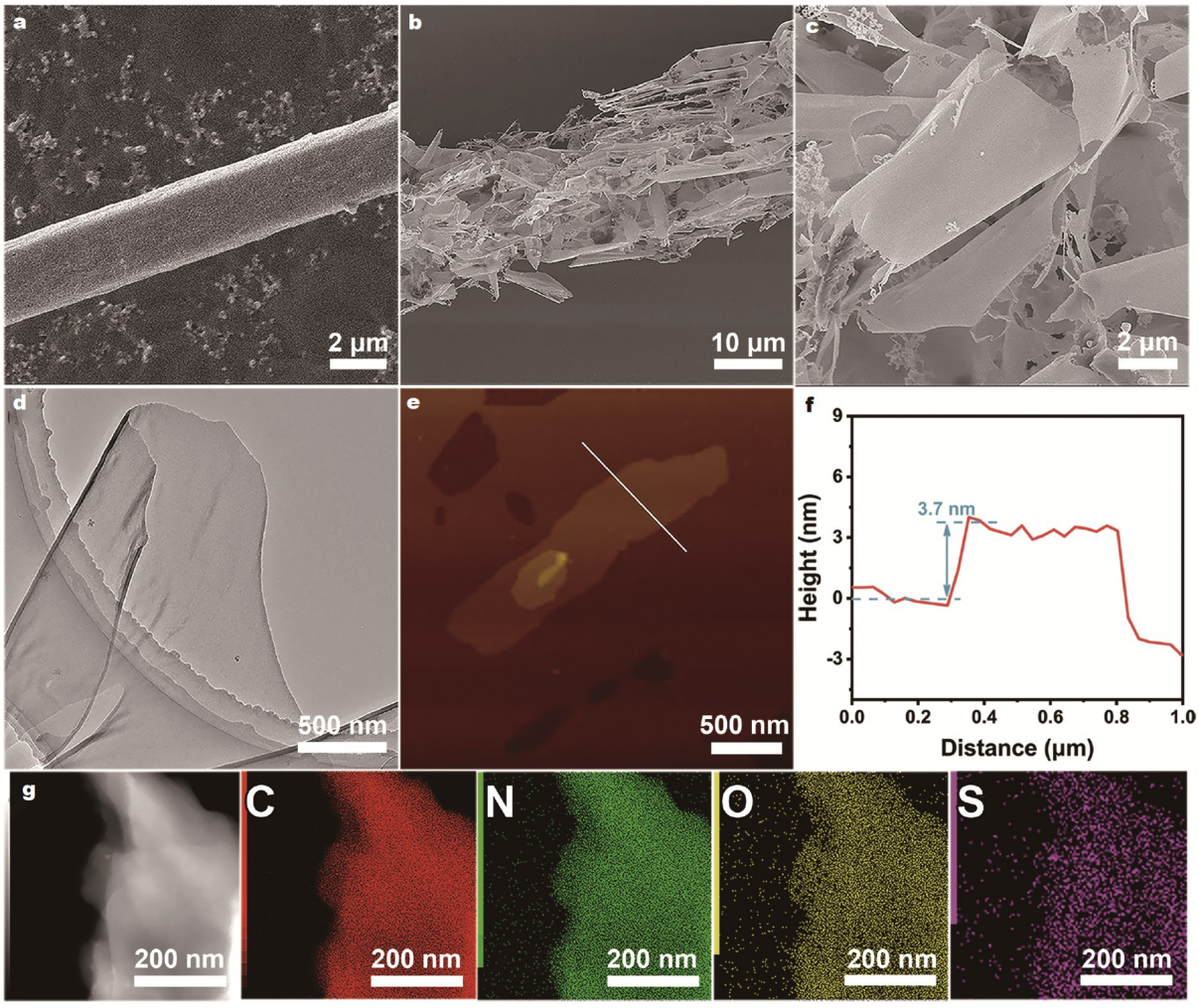

Figure 1 (a) SEM image of the precursor, (b, c) SEM images, (d) TEM image, (e) AFM image, and (f) the corresponding height profile along the white line of $SCN_{0.8}$. (g) TEM and the corresponding elemental mapping images of $SCN_{0.8}$.

charge transfer from the inside to the surface. Comparing the SEM images of SCN and its precursors with different S doping amounts (Figs S1 and S5), it is evident that the S introduction has a crucial effect on changing the morphology of the samples.

The crystal and chemical structures of BCN and $SCN_{0.8}$ were obtained using X-ray diffraction (XRD) measurements (Fig. 2a). $SCN_{0.8}$ and BCN exhibit two distinct diffraction peaks at 13.1° and 27.4°. The diffraction peak at 13.1° attributed to the in-plane arrangement of the aromatic rings corresponds to the (100) crystal plane. Furthermore, the diffraction peak at 27.4° attributed to the stacking mode between layers corresponds to the (002) crystal plane, indicating that $SCN_{0.8}$ maintains the basic structure of g-C_3N_4. The peak intensity of 13.1° and 27.4° for $SCN_{0.8}$ is considerably lower than that of BCN, which can be attributed to the ultrathin structure and S doping of $SCN_{0.8}$. Both factors can affect the interlayer period length in the graphitic layer and break the in-plane network orderliness. The chemical structures of $SCN_{0.8}$ and BCN were investigated using Fourier transform infrared spectroscopy (FTIR), as depicted in Fig. 2b. The sharp peak at 807 cm^{-1} and the band at 1200–1650 cm^{-1} correspond to the breathing vibration of the triazine units and stretching vibrations of C–N and C=N, respectively. These two characteristic absorptions resemble those of BCN. Another wider band at 2900–3300 cm^{-1} is attributed to the hydrogen-bonding vibrational region of –NH and –OH. The above results indicate that $SCN_{0.8}$ has well maintained the short-range structure of g-C_3N_4, and S doping does not break the structure.

As shown in Fig. 2c, the specific surface area of $SCN_{0.8}$ (139.06 $m^2 g^{-1}$) is 21 times higher than that of BCN (6.34 $m^2 g^{-1}$), which is beneficial for $SCN_{0.8}$ to expose more catalytically active sites. To determine the electronic characteristics of BCN and $SCN_{0.8}$, room-temperature electron paramagnetic resonance (EPR) spectra were characterized (Fig. 2d). Both the samples exhibit similar symmetric EPR signals at a *g*-factor of 2.00 because of the unpaired electrons in their backbone [57]. Compared with BCN, $SCN_{0.8}$ exhibits a higher concentration of unpaired electrons due to the structural damage caused by the interaction of S doping with the nanosheet shape, forming more defects. The electron redistribution in the $SCN_{0.8}$ structure positively affects the separation and migration of photoinduced carriers, thereby enhancing the efficiency of visible-light hydrogen production.

The external chemical compositions of BCN and $SCN_{0.8}$ were analyzed using X-ray photoelectron spectroscopy (XPS) (Fig. 3a–c). The XPS wide spectra (Fig. S6) exhibit three spikes corresponding to the C 1s, N 1s, and O 1s signals, and the

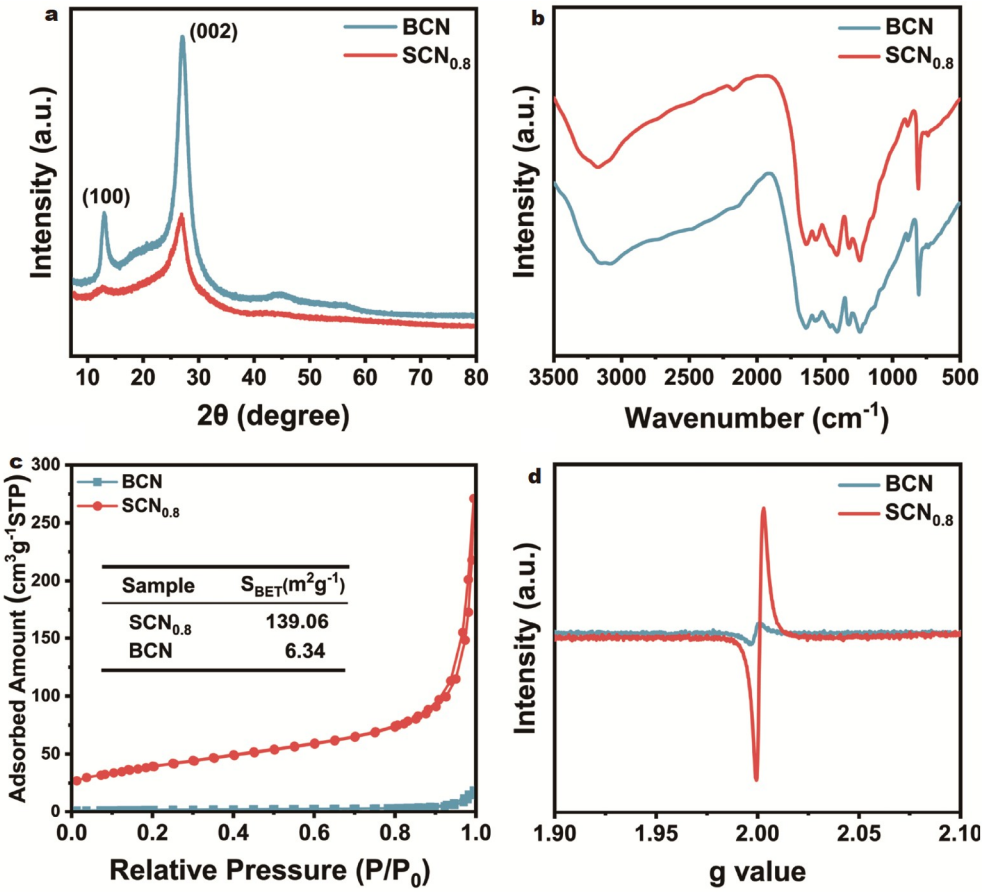

Figure 2 (a) XRD patterns, (b) FTIR, (c) nitrogen adsorption-desorption isotherms, and (d) room-temperature EPR spectra (25°C) of BCN and $SCN_{0.8}$.

measured spectrum of $SCN_{0.8}$ reveals the presence of the S 2p signal. Furthermore, the C 1s spectrum of $SCN_{0.8}$ can be deconvoluted into three peaks (Fig. 3a). The binding energy of 284.6 eV represents a characteristic peak of amorphous carbon (C–C/C=C). The two peaks at the binding energies of 285.9 and 287.9 eV represent the C–O bond and the sp^2-hybridized C atom (N–C=N) in the heterocycle, respectively. The peak intensity in the C 1s spectrum of $SCN_{0.8}$ at the binding energy of 285.9 eV is slightly increased and is preliminarily determined to contain C–S bonds [58].

Based on the findings presented in Fig. 3b, the N 1s spectrum of $SCN_{0.8}$ exhibits three distinct peaks at 398.1, 399.5, and 400.6 eV. These peaks can be attributed to the presence of sp^2-hybridized nitrogen in the nitrogen-containing aromatic ring (C–N=C), tertiary nitrogen group (N–$(C)_3$), and surface terminal amino groups (C–NH). SCN is inevitably doped with a small amount of oxygen (Fig. S7), arising from urea and cyanuric acid. In the O 1s spectrum of $SCN_{0.8}$, the two peaks correspond to the surface-adsorbed hydroxyl groups (531.4 eV) and the lattice oxygen (533.3 eV) of the C–O species. As shown in Fig. 3c, the S 2p spectrum of $SCN_{0.8}$ exhibits four peaks corresponding to $2p_{1/2}$ (166.2 eV) and $2p_{3/2}$ (164.1 eV) of the C–S–C bond formed when nitrogen atoms in the aromatic ring are replaced by S atoms, respectively, consistent with the C 1s result. Due to some physically adsorbed O_2, the peaks at 170.4 and 168.7 eV assigned to S–O bond appear during calcination. The above results indicate that S is successfully doped into the $SCN_{0.8}$ sample. Because N atoms are more electronegative than C atoms, C atoms act as electron donors. The electron densities around the C and O atoms in $SCN_{0.8}$ increase when the N atoms in N–C=N are replaced by S atoms, which have lower electronegativity.

Fig. 3d depicts the surface work functions (φ) of BCN and $SCN_{0.8}$, where $SCN_{0.8}$ exhibits a higher work function value, suggesting that the approximate Fermi level of $SCN_{0.8}$ is lower than that of BCN. This difference in Fermi levels affects the built-in electric field and surface band bending. In addition, the lower Fermi level facilitates the efficient transfer of photogenerated electrons to the surface, causing a substantial decrease in electron-hole recombination [59].

Ultraviolet-visible (UV-vis) diffuse reflectance spectroscopy is a common method that measures the light absorption capabilities of semiconductors. Fig. S8 depicts the UV-vis spectrum of SCN samples with different S content. Compared with other samples, $SCN_{0.8}$ has a better absorption capacity for visible light. The π–π* transition in heterocyclic aromatic hydrocarbons can be activated within the wavelength range of 300–370 nm. BCN typically exhibits the absorption of visible light, with an absorption edge around 455 nm. The band gap energy (E_g) decreases from 2.70 eV for BCN to 2.51 eV for $SCN_{0.8}$, as depicted in Fig. 4a (inset). The above results indicate that doping S into the framework of g-C_3N_4 shortens the band gap. Due to the deformed structure, the broadened absorption of approximately 500 nm of the $SCN_{0.8}$ photocatalyst is distributed to the n–π* excitations [60]. To determine the band structures of the samples before and after S doping, Mott–Schottky diagrams

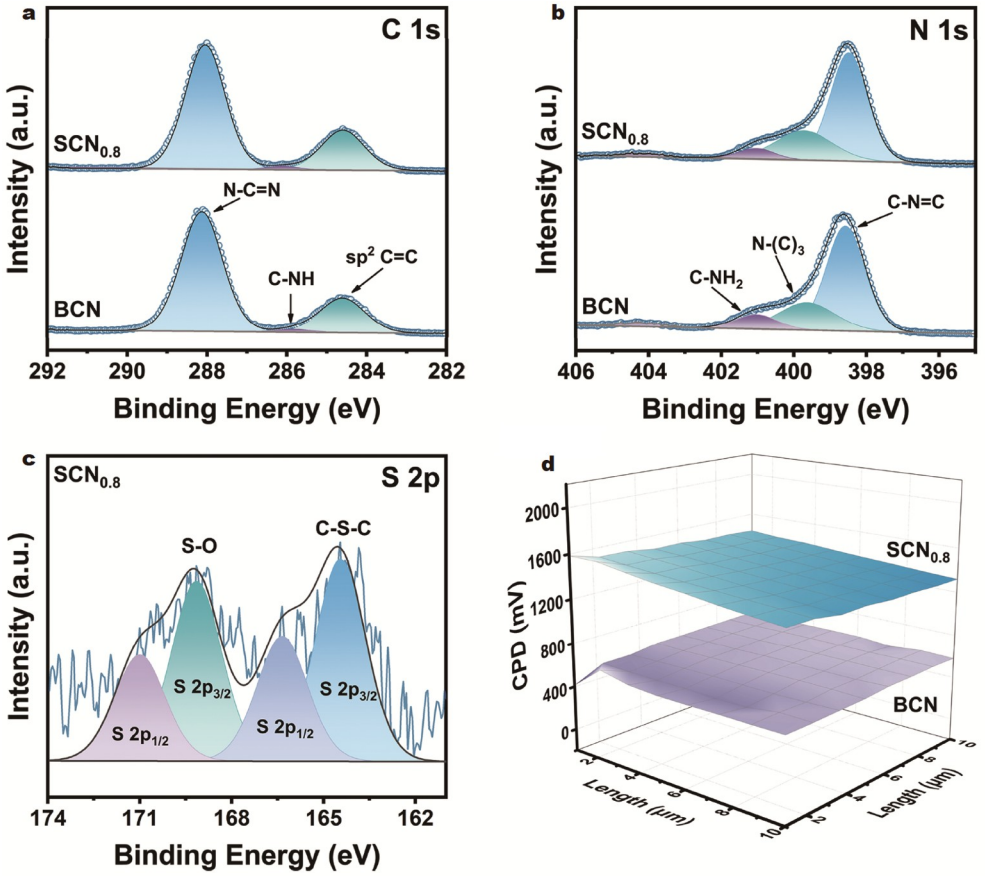

Figure 3 High-resolution XPS spectra of (a) C 1s and (b) N 1s obtained from BCN and $SCN_{0.8}$, respectively. High-resolution XPS spectrum of (c) S 2p obtained from $SCN_{0.8}$. (d) Contact potential differences (CPD) of BCN and $SCN_{0.8}$ relative to a gold reference.

were used to analyze their conduction band (CB) potentials (E_{CB}) (Fig. 4b, c). Both $SCN_{0.8}$ and BCN exhibit positive slopes, consistent with the characteristics of conventional n-type semiconductors [17]. The difference between CB potential and flat-band potential is very subtle. From the intersections, the flat-band potentials of BCN and $SCN_{0.8}$ are obtained as −1.21 V (*vs.* Ag/AgCl) and −1.05 V (*vs.* Ag/AgCl), respectively. For the E_g measured by UV-vis, the formula $E_{VB} = E_g + E_{CB}$ (1) can be utilized to calculate the valence band potentials (E_{VB}) of BCN and $SCN_{0.8}$, respectively, to be 1.49 and 1.46 eV. Fig. 4d shows the corresponding band structure arrangement of BCN and $SCN_{0.8}$, indicating that the CB of $SCN_{0.8}$ can reduce H^+ to H_2 thermodynamically.

The first principles of BCN and SCN were calculated by density functional theory. Melon-type carbon nitride was the calculated model for the imperfect polymerization of g-C_3N_4. To determine the role of S doping in the framework, S atoms were introduced into the single cell of BCN according to the structure analysis of SCN. Fig. 5a, d present the geometric structures of BCN and SCN after optimization, respectively. As depicted in Fig. 5b, e, the total density of states (DOS) and the projected DOS of BCN and SCN were analyzed in several ways. As shown in the Fig. 5c, f, the band gap value of SCN (2.44 eV) is reduced compared with that of BCN (2.65 eV), which is consistent with that of UV-vis (Fig. 4a). Narrow band gap can be caused by doping levels or distorted crystal structures [22]. The lower band gap facilitates the transfer of electrons from the N 2p orbital to the CB band and effectively broadens the light absorption range. These findings suggest that introducing S atoms into the carbon nitride framework is viable for enhancing its absorption of visible light.

Furthermore, to enhance the light-harvesting ability and narrow the band gap, the efficiency of separating and transferring photoinduced electron-hole pairs in photocatalysts plays a crucial role in identifying photocatalytic performance. As described in Fig. 6, optoelectronic testing and photoluminescence (PL) techniques were used to check the charge carrier separation and transfer efficiency in $SCN_{0.8}$. Fig. 6a depicts the transient photocurrent response results of BCN and $SCN_{0.8}$. Compared with BCN, the photoelectrode of $SCN_{0.8}$ demonstrates a higher photocurrent response, indicating enhanced separation and transfer of photogenerated charges. This phenomenon can be explained by adopting intermediate levels through S heteroatoms, which serve as trapping centers for photogenerated electrons. This promotes the isolation of electrons and holes, leading to an extended lifetime and enhanced mobility of charge carriers. The result of electrochemical impedance spectroscopy (Fig. 6b) demonstrated that the arc radius of $SCN_{0.8}$ is considerably smaller than BCN, indicating that $SCN_{0.8}$ has an inferior resistance to light-induced charge carrier transfer. Fig. 6c shows the PL spectra of the BCN and $SCN_{0.8}$ samples at an excitation wavelength of 365 nm. The PL spectrum of BCN shows that the emission peak at 480 nm results from charge carrier recombination. The PL intensity of $SCN_{0.8}$ considerably decreases compared with BCN, suggesting that the rate of electron-hole recombination can be effectively suppressed

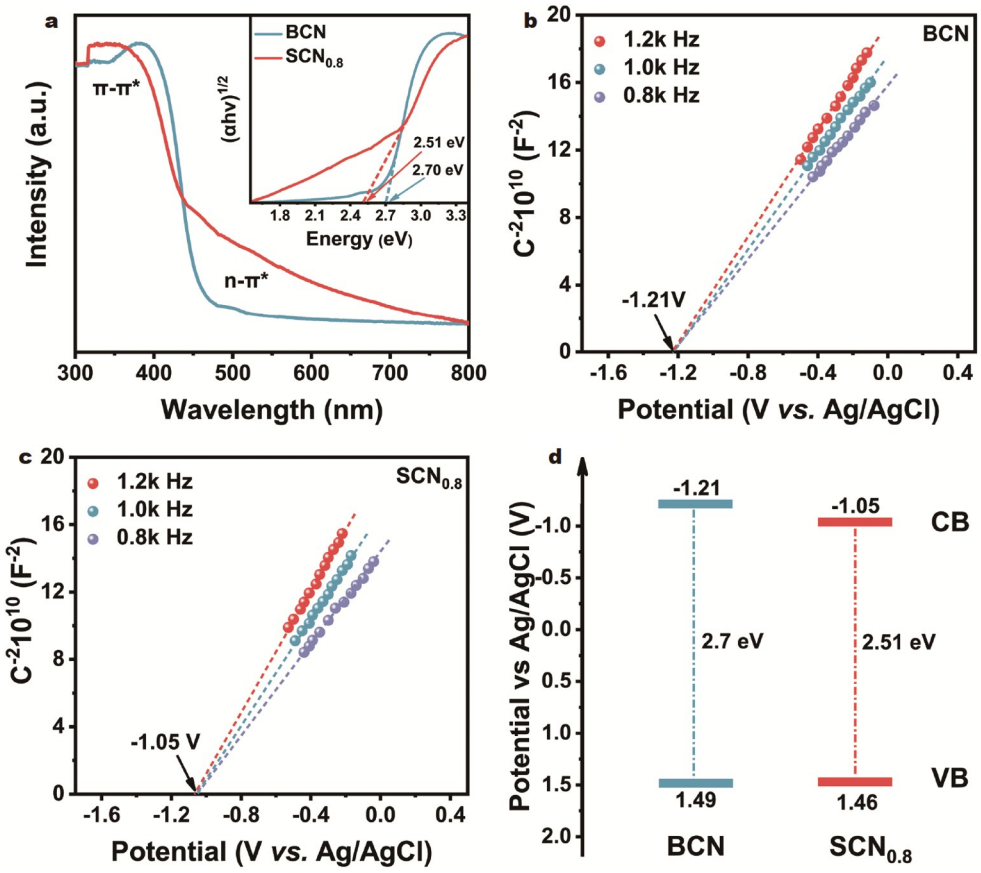

Figure 4 (a) UV-vis light absorption spectra and band gap energies of BCN and $SCN_{0.8}$. (b, c) Mott–Schottky plots of BCN and $SCN_{0.8}$ collected at various frequencies (recorded at pH 7). (d) Band edge alignments of BCN and $SCN_{0.8}$.

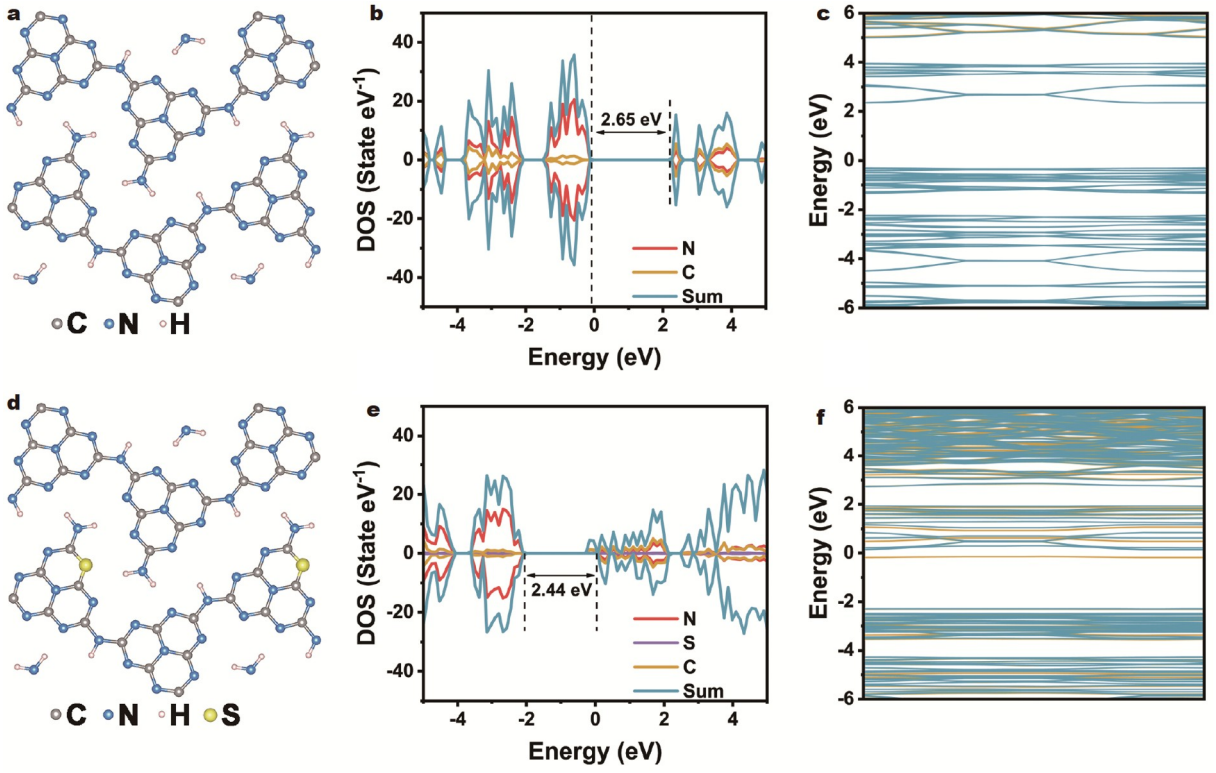

Figure 5 (a, d) Optimized structures, (b, e) calculated band structures, and (c, f) DOS of BCN and $SCN_{0.8}$.

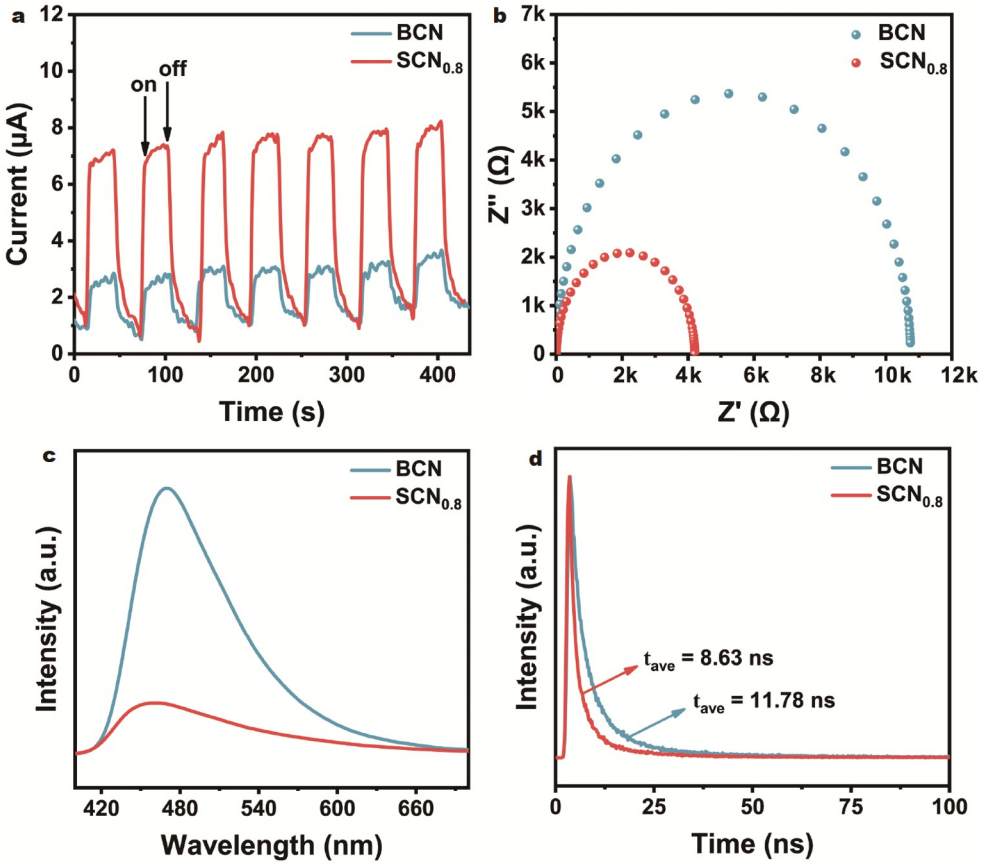

Figure 6 (a) Transient photocurrent responses, (b) Nyquist plots, (c) steady-state PL spectra and (d) TRPL spectroscopy with the corresponding fitting results of BCN and $SCN_{0.8}$.

in $SCN_{0.8}$. Time-resolved PL (TRPL) spectroscopy investigated the charge carrier separation and mobility, as depicted in Fig. 6d and Table S1. $SCN_{0.8}$ demonstrates a faster exponential decay, resulting in an average lifetime of 8.63 ns. The shorter lifetime of $SCN_{0.8}$ suggests a swift transfer of charge carriers, which is beneficial for improving photocatalytic activity.

To investigate the photocatalytic performance of the synthesized materials, we used a sacrificial agent of 10 vol% lactic acid and a cocatalyst of 2 wt% Pt. The photocatalytic experiments were performed using visible-light irradiation. The hydrogen evolution rate of SCN samples exhibits variation with the TU content in the precursor and is found to be considerably higher than that of BCN (Fig. 7). Notably, $SCN_{0.8}$ demonstrates an impressive H_2 release rate of 3925.8 μmol g^{-1} h^{-1}, surpassing BCN by 8.1 times (485.2 μmol g^{-1} h^{-1}). This hydrogen production rate is higher than most reported C_3N_4-based photocatalysts, as summarized in Table S2. There are several reasons why the hydrogen evolution rate of $SCN_{0.8}$ is higher than that of BCN. First, $SCN_{0.8}$ has a larger surface area, which increases the number of reactive sites. Second, the ultrathin and coiled nanosheets of $SCN_{0.8}$ shorten the diffusion paths of charges and protons and minimize the recombination with holes. Finally, incorporating S atoms into the g-C_3N_4 skeleton reduces the band gap and expands the range of visible-light absorption. The intensive photocatalytic performance results from the synergy effect of ultrathin nanosheet morphology and electronic modification induced by S doping.

The photocatalytic water splitting activities of photocatalysts with different S doping amounts were investigated, and the results are depicted in Fig. 7a, c. Specifically, only urea and cyanuric acid were selected as raw materials in the precursor synthesis process when no S source was added, and the hydrogen production rate of SCN_0 could only reach 1180.1 μmol g^{-1} h^{-1}. When a smaller amount of S was introduced, the hydrogen production rate of $SCN_{0.4}$ increased slightly to 2845.0 μmol g^{-1} h^{-1}. However, the hydrogen production rate of $SCN_{0.8}$ increased to 3925.8 μmol g^{-1} h^{-1} when the S content was increased. Further increasing the S content, $SCN_{1.6}$ showed the lowest hydrogen production rate only of 840.5 μmol g^{-1} h^{-1}. The introduction of a higher content of S may cause the S atom to become the center for reorganizing photogenerated charge carriers, which can inhibit the hydrogen evolution reaction. All samples were subjected to elemental analysis to assess the effect of the S concentration on the hydrogen evolution rate. As shown in Table S3, the content of S increases with the addition of TU. The addition of S does not enhance hydrogen evolution performance, according to a comprehensive analysis of the hydrogen evolution rate of all samples. The influence of individual Pt contents on the photocatalytic performance was examined, and the optimization results are depicted in Fig. 7b, d. The Pt loading of 2% (3925.8 μmol g^{-1} h^{-1}) on $SCN_{0.8}$ showed the highest activity than that of 1% (2880.3 μmol g^{-1} h^{-1}) and 3% (2020.1 μmol g^{-1} h^{-1}). The enhanced activity with 2% Pt loading may be due to the advanced concentration of Pt active sites

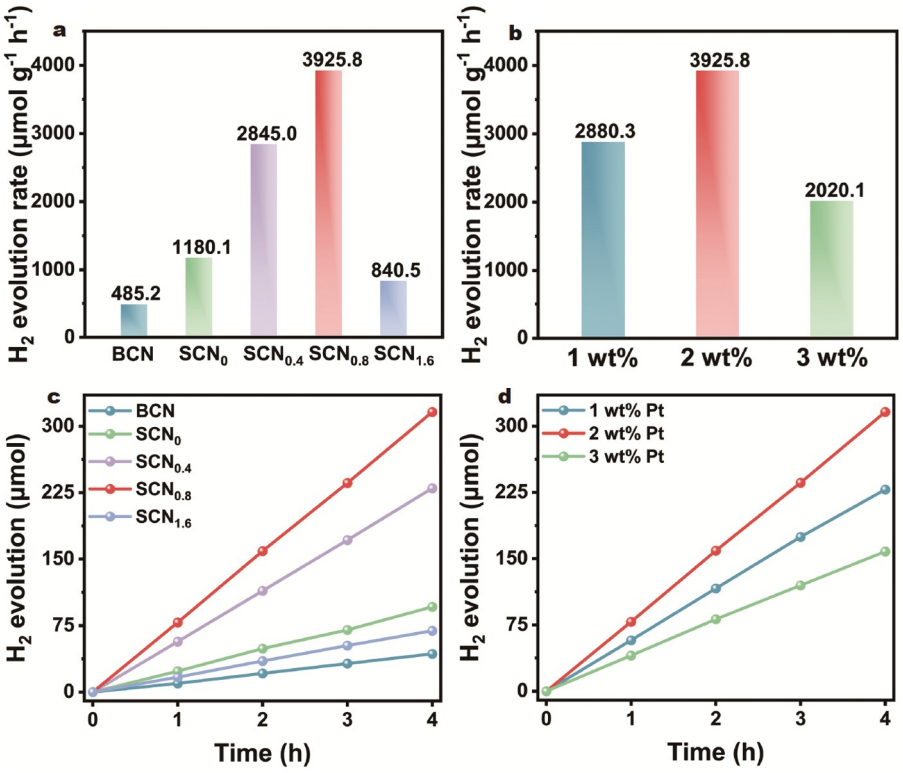

Figure 7 (a) Photocatalytic H_2 evolution rates of BCN and SCN photocatalysts under simulated sunlight (AM1.5). (b) Photocatalytic H_2 evolution rates of $SCN_{0.8}$ under simulated sunlight (AM1.5) with different Pt contents. (c) Photocatalytic H_2 evolution activities of BCN and SCN photocatalysts under simulated sunlight (AM1.5). (d) Photocatalytic H_2 evolution activities of $SCN_{0.8}$ under simulated sunlight (AM1.5) with different Pt contents.

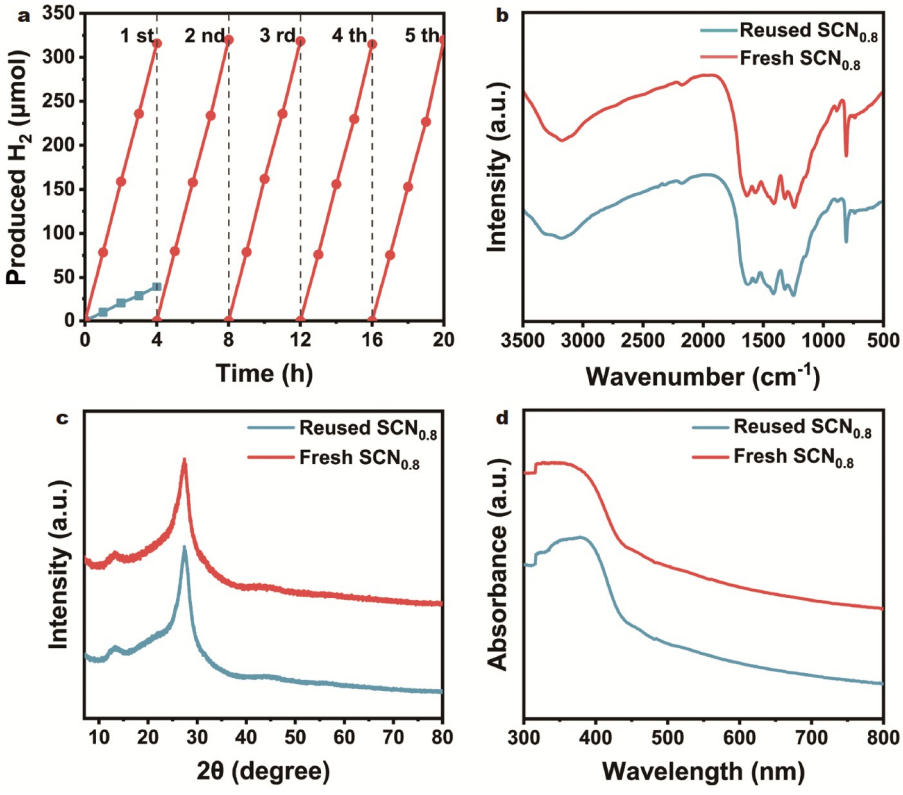

Figure 8 (a) Time course of H_2 evolution for BCN and $SCN_{0.8}$ under AM1.5 irradiation. (b) FTIR spectra, (c) XRD patterns, and (d) UV-vis light absorption spectra of $SCN_{0.8}$ before and after photocatalytic H_2 evolution under visible-light irradiation.

virtual for the proton reduction reaction. However, the performance decreased when Pt was further increased to 3%. The reduction in performance can be attributed to the capping impact, which hinders the light absorption and shields the exterior active sites.

The H_2 yield did not considerably decay after five cycle tests within a 20-h photocatalytic period (Fig. 8a). Fig. 8b, c compare the IR spectra and XRD patterns before and after the hydrogen evolution reaction. The crystal structure and chemical composition of $SCN_{0.8}$ remain unchanged after the photocatalytic reaction. Furthermore, the UV-vis absorption remains similar after the reaction (Fig. 8d), suggesting that the light-collecting ability of the photocatalytic material is unaffected, and the above results indicate that the $SCN_{0.8}$ sample exhibits high stability and sustainability under the applied reaction conditions.

CONCLUSION

We fabricated rod-shaped SCN nanosheet aggregates using self-assembling urea, TU, and cyanuric acid. Compared with BCN, $SCN_{0.8}$ demonstrates a considerable improvement in specific surface area, increased ability to absorb visible light, and an optimized electron and band gap structure. The photocatalytic hydrogen production rate of $SCN_{0.8}$ is nearly 8.1 times that of BCN, and the catalytic activity remains good after the cyclic stability test. The prominent catalytic performance can be attributed to the synergistic effect of ultrathin nanosheets and the S doping structure. This research not only provides a novel experimental concept for the self-assembly strategy to synthesize heteroatom-doped g-C_3N_4 for stable and high-performance photocatalytic hydrogen production, but also proposes a promising general approach for the simultaneous regulation of nanostructure and electronic structure of g-C_3N_4 during one-step pyrolysis of supramolecular precursors.

Received 30 August 2023; accepted 19 September 2023; published online 9 November 2023

1 Ong WJ, Tan LL, Ng YH, *et al.* Graphitic carbon nitride (g-C_3N_4)-based photocatalysts for artificial photosynthesis and environmental remediation: Are we a step closer to achieving sustainability? Chem Rev, 2016, 116: 7159–7329
2 Kofuji Y, Ohkita S, Shiraishi Y, *et al.* Graphitic carbon nitride doped with biphenyl diimide: Efficient photocatalyst for hydrogen peroxide production from water and molecular oxygen by sunlight. ACS Catal, 2016, 6: 7021–7029
3 Dong J, Gong Z, Chen Y, *et al.* Organic microstructure-induced hierarchically porous g-C_3N_4 photocatalyst. Sci China Mater, 2023, 66: 3176–3188
4 Zeng Z, Yu H, Quan X, *et al.* Structuring phase junction between tri-*s*-triazine and triazine crystalline C_3N_4 for efficient photocatalytic hydrogen evolution. Appl Catal B-Environ, 2018, 227: 153–160
5 Lin L, Yu Z, Wang X. Crystalline carbon nitride semiconductors for photocatalytic water splitting. Angew Chem Int Ed, 2019, 58: 6164–6175
6 Jiang N, Wang H, Luo Y, *et al.* Facile two-step treatment of carbon nitride for preparation of highly efficient visible-light photocatalyst. Appl Catal B-Environ, 2018, 227: 541–547
7 Zheng Y, Lin L, Wang B, *et al.* Graphitic carbon nitride polymers toward sustainable photoredox catalysis. Angew Chem Int Ed, 2015, 54: 12868–12884
8 Chen S, Yang Z, Chen J, *et al.* Electron-rich interface of Cu-Co heterostructure nanoparticle as a cocatalyst for enhancing photocatalytic hydrogen evolution. Chem Eng J, 2022, 434: 134673
9 Yang Z, Li M, Chen S, *et al.* Cocatalyst engineering with robust tunable carbon-encapsulated Mo-rich Mo/Mo_2C heterostructure nanoparticle for efficient photocatalytic hydrogen evolution. Adv Funct Mater, 2023, 33: 2212746
10 Zhou T, Li T, Hou J, *et al.* Tailoring boron doped intramolecular donor–acceptor integrated carbon nitride skeleton with propelling photocatalytic activity and mechanism insight. Chem Eng J, 2022, 445: 136643
11 Liu J, Li Q, Xiao X, *et al.* Metal-organic frameworks loaded on phosphorus-doped tubular carbon nitride for enhanced photocatalytic hydrogen production and amine oxidation. J Colloid Interface Sci, 2021, 590: 1–11
12 Xiao X, Gao Y, Zhang L, *et al.* A promoted charge separation/transfer system from Cu single atoms and C_3N_4 layers for efficient photocatalysis. Adv Mater, 2020, 32: 2003082
13 Wu B, Zhang L, Jiang B, *et al.* Ultrathin porous carbon nitride bundles with an adjustable energy band structure toward simultaneous solar photocatalytic water splitting and selective phenylcarbinol oxidation. Angew Chem Int Ed, 2021, 60: 4815–4822
14 Zhao C, Li Q, Xie Y, *et al.* Three-dimensional assemblies of carbon nitride tubes as nanoreactors for enhanced photocatalytic hydrogen production. J Mater Chem A, 2020, 8: 305–312
15 Li Q, Zhang L, Liu J, *et al.* Porous carbon nitride thin strip: Precise carbon doping regulating delocalized π-electron induces elevated photocatalytic hydrogen evolution. Small, 2021, 17: 2006622
16 Liu D, Li C, Zhao C, *et al.* Facile synthesis of three-dimensional hollow porous carbon doped polymeric carbon nitride with highly efficient photocatalytic performance. Chem Eng J, 2022, 438: 135623
17 Xiao Y, Tian G, Li W, *et al.* Molecule self-assembly synthesis of porous few-layer carbon nitride for highly efficient photoredox catalysis. J Am Chem Soc, 2019, 141: 2508–2515
18 Li Y, Jin R, Xing Y, *et al.* Macroscopic foam-like holey ultrathin g-C_3N_4 nanosheets for drastic improvement of visible-light photocatalytic activity. Adv Energy Mater, 2016, 6: 1601273
19 Schwinghammer K, Mesch MB, Duppel V, *et al.* Crystalline carbon nitride nanosheets for improved visible-light hydrogen evolution. J Am Chem Soc, 2014, 136: 1730–1733
20 Chen X, Shi R, Chen Q, *et al.* Three-dimensional porous g-C_3N_4 for highly efficient photocatalytic overall water splitting. Nano Energy, 2019, 59: 644–650
21 Xia P, Zhu B, Yu J, *et al.* Ultra-thin nanosheet assemblies of graphitic carbon nitride for enhanced photocatalytic CO_2 reduction. J Mater Chem A, 2017, 5: 3230–3238
22 Luo L, Gong Z, Ma J, *et al.* Ultrathin sulfur-doped holey carbon nitride nanosheets with superior photocatalytic hydrogen production from water. Appl Catal B-Environ, 2021, 284: 119742–119751
23 Tang C, Cheng M, Lai C, *et al.* Recent progress in the applications of non-metal modified graphitic carbon nitride in photocatalysis. Coord Chem Rev, 2023, 474: 214846
24 Wang H, Thangamuthu M, Wu Z, *et al.* Self-assembled sulphur doped carbon nitride for photocatalytic water reforming of methanol. Chem Eng J, 2022, 445: 136790
25 Patnaik S, Sahoo DP, Parida K. Recent advances in anion doped g-C_3N_4 photocatalysts: A review. Carbon, 2021, 172: 682–711
26 Chen Y, Yu M, Huang G, *et al.* Interlayer charge transfer over graphitized carbon nitride enabling highly-efficient photocatalytic nitrogen fixation. Small, 2022, 18: 2205388
27 Li J, Wu D, Iocozzia J, *et al.* Achieving efficient incorporation of π-electrons into graphitic carbon nitride for markedly improved hydrogen generation. Angew Chem Int Ed, 2019, 58: 1985–1989
28 Liu Q, Tian H, Dai Z, *et al.* Nitrogen-doped carbon nanospheres-modified graphitic carbon nitride with outstanding photocatalytic activity. Nano-Micro Lett, 2020, 12: 24
29 Liu Y, Tayyab M, Pei W, *et al.* The precision defect engineering with nonmetallic element refilling strategy in g-C_3N_4 for enhanced photocatalytic hydrogen production. Small, 2023, 19: 2208117
30 Jiang L, Yuan X, Pan Y, *et al.* Doping of graphitic carbon nitride for photocatalysis: A review. Appl Catal B-Environ, 2017, 217: 388–406
31 Fei T, Qin C, Zhang Y, *et al.* A 3D peony-like sulfur-doped carbon nitride synthesized by self-assembly for efficient photocatalytic hydro-

gen production. Int J Hydrogen Energy, 2021, 46: 20481–20491
32 Wang J, Jiang Z. Ultrasonic-assisted synthesis of porous S-doped carbon nitride ribbons for photocatalytic reduction of CO_2. Ultrasons SonoChem, 2023, 92: 106273
33 Wang L, Li R, Zhang Y, *et al.* Phosphorus doping to enhance the peroxymonosulfate activation efficiency of carbon nitride for degrading tetracycline. J Water Process Eng, 2023, 54: 103916
34 Ma TY, Ran J, Dai S, *et al.* Phosphorus-doped graphitic carbon nitrides grown *in situ* on carbon-fiber paper: Flexible and reversible oxygen electrodes. Angew Chem Int Ed, 2015, 54: 4646–4650
35 Zhao S, Liu Y, Wang Y, *et al.* A self-assembly strategy to synthesize carbon doped carbon nitride microtubes with a large π-electron conjugated system for efficient H_2 evolution. Chem Eng J, 2022, 447: 137436
36 Wang H, Huang G, Chen Z, *et al.* Carbon self-doped carbon nitride nanosheets with enhanced visible-light photocatalytic hydrogen production. Catalysts, 2018, 8: 366
37 Yang Y, Guo W, Zhai Y, *et al.* Oxygen-doped and nitrogen vacancy co-modified carbon nitride for the efficient visible light photocatalytic hydrogen evolution. New J Chem, 2020, 44: 16320–16328
38 Wang Y, Rao L, Wang P, *et al.* Porous oxygen-doped carbon nitride: Supramolecular preassembly technology and photocatalytic degradation of organic pollutants under low-intensity light irradiation. Environ Sci Pollut Res, 2019, 26: 15710–15723
39 Gu Q, Liu J, Gao Z, *et al.* Homogenous boron-doping in self-sensitized carbon nitride for enhanced visible-light photocatalytic activity. Chem — An Asian J, 2016, 11: 3169–3173
40 Bao H, Wang L, Li G, *et al.* Carrier engineering of carbon nitride boosts visible-light photocatalytic hydrogen evolution. Carbon, 2021, 179: 80–88
41 Liu Z, Ma J, Hong M, *et al.* Potassium and sulfur dual sites on highly crystalline carbon nitride for photocatalytic biorefinery and CO_2 reduction. ACS Catal, 2023, 13: 2106–2117
42 Liu G, Niu P, Sun C, *et al.* Unique electronic structure induced high photoreactivity of sulfur-doped graphitic C_3N_4. J Am Chem Soc, 2010, 132: 11642–11648
43 Qi Z, Chen J, Zhou W, *et al.* Synergistic effects of holey nanosheet and sulfur-doping on the photocatalytic activity of carbon nitride towards NO removal. Chemosphere, 2023, 316: 137813
44 Zhang J, Sun J, Maeda K, *et al.* Sulfur-mediated synthesis of carbon nitride: Band-gap engineering and improved functions for photocatalysis. Energy Environ Sci, 2011, 4: 675–678
45 Lv H, Huang Y, Koodali RT, *et al.* Synthesis of sulfur-doped 2D graphitic carbon nitride nanosheets for efficient photocatalytic degradation of phenol and hydrogen evolution. ACS Appl Mater Interfaces, 2020, 12: 12656–12667
46 Hong J, Xia X, Wang Y, *et al.* Mesoporous carbon nitride with *in situ* sulfur doping for enhanced photocatalytic hydrogen evolution from water under visible light. J Mater Chem, 2012, 22: 15006–15012
47 Zhang J, Guo F, Wang X. An optimized and general synthetic strategy for fabrication of polymeric carbon nitride nanoarchitectures. Adv Funct Mater, 2013, 23: 3008–3014
48 Huang Y, Zheng H, Li H, *et al.* Highly effective and selective adsorption of thorium(IV) from aqueous solution using mesoporous graphite carbon nitride prepared by sol-gel template method. Chem Eng J, 2021, 410: 128321
49 Guo S, Deng Z, Li M, *et al.* Phosphorus-doped carbon nitride tubes with a layered micro-nanostructure for enhanced visible-light photocatalytic hydrogen evolution. Angew Chem Int Ed, 2016, 55: 1830–1834
50 Cao S, Chen H, Jiang F, *et al.* Nitrogen photofixation by ultrathin amine-functionalized graphitic carbon nitride nanosheets as a gaseous product from thermal polymerization of urea. Appl Catal B-Environ, 2018, 224: 222–229
51 Zhang G, Zhang J, Zhang M, *et al.* Polycondensation of thiourea into carbon nitride semiconductors as visible light photocatalysts. J Mater Chem, 2012, 22: 8083–8091
52 Li Q, Ren C, Qiu C, *et al.* Promoting near-infrared photocatalytic activity of carbon-doped carbon nitride *via* solid alkali activation. Chin Chem Lett, 2021, 32: 3463–3468
53 Ran J, Ma TY, Gao G, *et al.* Porous P-doped graphitic carbon nitride nanosheets for synergistically enhanced visible-light photocatalytic H_2 production. Energy Environ Sci, 2015, 8: 3708–3717
54 Gao K, Wang B, Tao L, *et al.* Efficient metal-free electrocatalysts from N-doped carbon nanomaterials: Mono-doping and co-doping. Adv Mater, 2019, 31: 1805121
55 Makaremi M, Grixti S, Butler KT, *et al.* Band engineering of carbon nitride monolayers by n-type, p-type, and isoelectronic doping for photocatalytic applications. ACS Appl Mater Interfaces, 2018, 10: 11143–11151
56 Praus P, Smýkalová A, Foniok K, *et al.* Doping of graphitic carbon nitride with oxygen by means of cyanuric acid: Properties and photocatalytic applications. J Environ Chem Eng, 2021, 9: 105498
57 Qin J, Wang S, Ren H, *et al.* Photocatalytic reduction of CO_2 by graphitic carbon nitride polymers derived from urea and barbituric acid. Appl Catal B-Environ, 2015, 179: 1–8
58 Wang H, Bian Y, Hu J, *et al.* Highly crystalline sulfur-doped carbon nitride as photocatalyst for efficient visible-light hydrogen generation. Appl Catal B-Environ, 2018, 238: 592–598
59 Hu S, Qiao P, Zhang L, *et al.* Assembly of TiO_2 ultrathin nanosheets with surface lattice distortion for solar-light-driven photocatalytic hydrogen evolution. Appl Catal B-Environ, 2018, 239: 317–323
60 An S, Zhang G, Li K, *et al.* Self-supporting 3D carbon nitride with tunable n→π* electronic transition for enhanced solar hydrogen production. Adv Mater, 2021, 33: 2104361

Acknowledgements This work was supported by the National Natural Science Foundation of China (52273264), the Outstanding Youth Fund of Heilongjiang Province (JQ 2020B002), and the Basic Scientific Research Services of Colleges and Universities of Heilongjiang Province (2022-KYYWF-1107). We thank Dr. Hongsen Zhang of Harbin Engineering University for providing XPS testing services.

Author contributions Lin S and Jiang B designed and performed the experiments and wrote the paper; Li Q carried out the theoretical calculation; Wu B conducted the experiment guidance and article modification; Liu J participated in part of the experimental characterization; Zheng M and Xiao X provided the experiment guidance; Xie Y assisted in the theoretical calculation; Lin S wrote the paper with support from Jiang B and Wu B. All authors contributed to the general discussion.

Conflict of interest The authors declare that they have no conflict of interest.

Supplementary information Experimental details and supporting data are available in the online version of the paper.

Siying Lin is a doctoral student at the School of Chemistry and Materials Science, Heilongjiang University. Her current research interests include photocatalytic material synthesis.

Baogang Wu is a doctoral student at the School of Chemistry and Materials Science, Heilongjiang University. His current research interests include photocatalytic material synthesis.

Baojiang Jiang received his BS degree in 2001 from Heilongjiang University, China. In 2012, he received his PhD degree from Harbin Engineering University, China. He became a full professor in 2016 at the Heilongjiang University. His recent research interests include organic and inorganic semiconductor photocatalytic materials for renewable clean energy and environmental protection applications.

硫掺杂氮化碳纳米片棒状聚集体用于光催化析氢

林斯颖[1], 吴宝刚[1], 李琪[2], 肖旭东[1], 郑芒[2], 刘佳男[1], 谢颖[1], 蒋保江[1*]

摘要 合成具有较宽吸收光谱的少层氮化碳是一个具有吸引力的课题. 杂原子掺杂(特别是硫掺杂)可以有效地避免纳米级片层氮化碳中由于量子限制效应所引起的带隙加宽. 与二次煅烧硫化不同的是, 预硫化超分子前驱体可以原位地形成硫掺杂氮化碳纳米片堆叠聚集体(SCN). 这种少层的框架结构呈现出了更大的比表面积(139.06 $m^2 g^{-1}$), 暴露了更多的活性位点. 此外, 硫的引入使原七嗪环的共轭结构发生扭曲, 从而通过激活价带电子的n→π*跃迁而缩小带隙. 在模拟日光条件下, $SCN_{0.8}$ (3925.8 μmol $g^{-1} h^{-1}$)的析氢速率是块体氮化碳(BCN, 485.2 μmol $g^{-1} h^{-1}$)的8.1倍. 本工作旨在最大限度地利用杂原子掺杂和形态调控的协同效应来提高光催化活性, 且为光催化剂的多维同步优化提供了新的视角.